Influence of the crystallographic orientations of Ti–6Al–4V substrate on the morphology and optical properties of oxide thin films obtained by anodizing

Sarah Marion, Matthieu Lenci, Jules Galipaud, Clotilde Minfray, Vincent Fridrici, Jenny Faucheu, Charrière Renée

Influence of the crystallographic orientations of Ti-6Al-4V substrate on the morphology and optical properties of oxide thin films obtained by anodizing

S. Marion[a,b,*], M. Lenci[a], J. Galipaud[b], C. Minfray[b], V. Fridrici[b], J. Faucheu[a], R. Charrière[a]

[a] *Mines Saint-Etienne, Université de Lyon, CNRS, UMR 5307 LGF, Centre SMS, F-42023 Saint-Etienne France*
[b] *Laboratoire de Tribologie et Dynamique des Systèmes, UMR CNRS 5513 ECL ENTPE, Université de Lyon, Ecole Centrale de Lyon, F-69134 Ecully cedex*

Abstract

The origin of color inhomogeneity in anodized titanium at the microscopic scale is investigated. Oxide layers were produced by galvanostatic anodizing in sulfuric acid on commercial Ti-6Al-4V substrates, with and without HF/HNO_3 etching prior to anodizing. The crystallographic orientations of the Ti-6Al-4V substrates were determined using Electron Backscatter Diffraction (EBSD) before anodizing. The chemical composition of the oxide thin films was characterized using X-ray Photoelectron Spectroscopy (XPS). The oxide thin films were observed optically using a digital microscope. The internal morphology of the oxide layers was observed through a Scanning Transmission Electron Microscope (STEM) on Focused Ion Beam (FIB) lamella preparations, taken at the boundary of two differently colored areas on anodized Ti-6Al-4V samples. By characterizing both the substrate and the oxide layer, a correlation was established between the crystallographic orientations of the underlying Ti-6Al-4V substrate and the morphology of the oxide layer. It is shown that crystallographic orientations of the α phase of the substrate close to the basal plane (0001) lead to a porous oxide layer, resulting in a blue color. For other α grains and the β grains of the substrate, the oxide layer is dense and exhibits a yellow color. The development of an optical model to simulate color, accounting for the porosity of the oxide layer, confirms the correlation between porosity and color.

Keywords: titanium alloy, electron backscattered diffraction (EBSD), anodizing, porosities, color

1. Introduction

Titanium is attracting more and more attention in the luxury industry (jewelry, watches, packaging). Titanium has low density, high stiffness and is efficiently shaped through additive manufacturing enabling designers to create large objects with complex shapes. Moreover, titanium is also hypoallergenic and can exhibit a variety of metallic-colored aspects through oxidation. These colored aspects result from the formation of a thin layer of transparent titanium oxide on the titanium surface, leading to interferential optical phenomena responsible for the perceived color [1, 2, 3]. It has been demonstrated that color depends on the thickness [1, 4] and refractive indexes of the substrate [5] and oxide layer [2]. The oxide layer's refractive index varies with the oxide crystalline structure [1, 3, 6] and composition. The TiO_2 films can be produced through various techniques, such as thermal oxidation [7, 8], laser oxidation [9], magnetron sputtering [10, 11, 12] and anodizing [13]. Among these techniques, anodizing stands out for its ability to generate oxide layers with a thickness of hundreds of nanometers [14], or even, under specific experimental conditions, nanotubes with a length of several tens of micrometers [15] while requiring few equipments and being fast and inexpensive. In galvanostatic mode, a linear relationship between cell voltage and the oxide thickness is usually established. The growth rate of the oxide layer, defined as the ratio of oxide thickness to the maximum voltage reached during the process, varies from 1.5 to 3 nm/V [14, 16] and depends on various anodizing parameters such as current density, electrolyte composition, temperature, surface preparation and metal composition [14, 17]. The color of anodized titanium is perceived as homogeneous at the macroscopic scale [18, 19, 20]. But closer observations at the microscopic scale on anodized titanium have revealed color heterogeneities with one color being predominantly present and small areas of other colors being evenly distributed, showing variations in hue and shade [4, 21]. A correlation between the crystallographic orientations of the Ti [21] or Ti-6Al-4V [4] substrates

*Corresponding author.
Email address: sarah.marion@emse.fr (S. Marion)

and the resulting color after anodizing has been demonstrated. In addition, Diamanti et al. [21] have shown that oxide thicknesses are reduced when grown on grains with crystallographic orientations of the α phase near (0001), resulting in color variations. Moreover, several studies [22, 23] have shown that the growth rate of TiO_2 nanotubes is influenced by the crystallographic orientations of the substrate on which they grow. The variation in growth rate is explained by the different atomic densities of the planes, which lead to different oxidation rates [22].

However, the influence of crystallographic orientations on oxide layer growth, particularly on its morphology, remains unclear partly due to the lack of information on the internal morphology of the oxide layer. Until now, previous studies on anodized titanium have not paid attention to the internal morphology of the oxide layer. Notably, authors have usually relied on the assumption of a dense layer to estimate the oxide thickness according to the local sample color [4, 21]. However, it should be noted that the oxide layer can be porous [2, 24]. For the same oxide thickness, different porosity fractions can produce different colors by modifying the effective refractive index of the oxide layer.

Consequently, this article aims to examine how the crystallographic orientations of the Ti-6Al-4V substrate influence the morphology of the oxide layer obtained through anodizing, with regard to the resulting optical properties. Chemical, microstructural and optical characterizations were carried out. Moreover, the internal morphology of the oxide layer was observed through a Scanning Transmission Electron Microscope (STEM) on Focused Ion Beam (FIB) lamella preparations, taken at the boundary of two differently colored areas on anodized Ti-6Al-4V samples.

2. Material and methods

2.1. Substrate

The substrates used in this study are flat samples of a commercial Ti-6Al-4V alloy purchased from Acnis International (grade 23 in ASTM F136-13, ISO 5832-3:2021). The dimensions of the samples are 15 x 20 mm^2 with a thickness of 2 mm. The chemical composition is given in Table 1. The alloy was produced by hot rolling in the annealed state, resulting in a microstructure comprising two phases: an α phase, which is aluminum-rich, and a β phase, which is vanadium-rich. These phases have hexagonal close-packed (hcp) and body-centered cubic (bcc) crystal structures, respectively.

Table 1: Chemical composition of the Ti-6Al-4V substrates from [25], the values are given in weight percentage.

weight %	O	Fe	C	H	N	Al	V	Ti
min	—	—	—	—	—	5.5	3.5	balance
max	0.13	0.25	0.08	0.012	0.05	6.5	4.5	

The Ti-6Al-4V substrates were polished with SiC abrasive papers with decreasing granulometry from P240 to P2400 lubricated with water. Then, they were polished with 0.06 µm colloidal silica with alumina suspensions and hydrogen peroxide at 4 % (v/v) to achieve a mirror surface (arithmetical mean height of the surface, $S_a = 30$ nm). Subsequently, the surface was cleaned with water and detergent, rinsed with ethanol and dried with hot air.

Indentations were made on the substrate surface using a Vickers hardness indenter to identify the analysis area and enable all characterizations to be performed in the same area (Figure 1). Additionally, the samples were polished by vibration with 0.06 µm colloidal silica to reduce the stresses induced by mechanical polishing and indentations on the surface, leading to better indexing, particularly of the β phase during Electron BackScatter Diffraction (EBSD) analysis.

Two surface preparations were investigated: one substrate underwent anodizing after vibratory polishing and surface cleaning with water and detergent, rinsing with ethanol, and drying with hot air (designated as "not etched"), while the other underwent etching with an aqueous solution of HF (5 wt%) and HNO_3 (20 wt%) for 15 seconds before anodizing (designated as "etched").

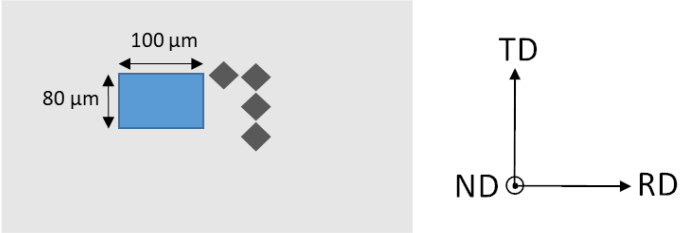

Figure 1: Schematic of the studied area (blue rectangle) where RD is the rolling direction, TD is the transverse direction to the rolling direction and ND is the normal direction to the rolling direction. Scale is not respected.

2.2. Synthesis of oxide thin films

The oxide thin films were produced through anodizing. The samples were anodized at room temperature (25°C) by applying a DC electric current between an activated Ti cathode and Ti-6Al-4V anode. The electrolyte used was a sulfuric acid H_2SO_4 solution with a concentration of 0.5 mol/L. A voltage of 50 V was applied (corresponding to an approximative oxide thickness of 120 nm [14]). The current density was kept constant at 20 mA/cm^2 (galvanostatic mode) until reaching the preset voltage. After 30 seconds, the anodizing was stopped, and the samples were washed with demineralized water and dried using compressed air. In the remainder of this article, the samples will be referred to as "ANOD-50V" for the anodized not etched substrate and "ANOD-50V-HF" for the anodized etched substrate.

2.3. Characterizations

Characterizations of both the substrates and the oxide thin films were carried out to study the influence of the crystallographic orientations of the substrate on the formation of the oxide thin film and the perceived color.

Firstly, the substrates were characterized using the EBSD technique on the two surface preparations (unetched and etched) using a ZEISS Scanning Electron Microscope (SEM) with a field emission gun. The Symmetry S2 detector was used to collect data at 2500x magnification over an area of 100 x 80 µm^2 on the (RD, TD) orientation face (Figure 1) with a step size of 0.25 µm and a frequency of 50 Hz. Data analysis was performed through custom MATLAB scripts using functions from the MTEX package [26].

Then, chemical, microstructural and optical characterizations of the oxide layer were carried out at the microscopic scale. X-ray Photoelectron Spectroscopy (XPS) was used for chemical surface analysis, using a Ulvac-Phi Versaprobe II Kα X-ray photoelectron spectrometer with focused monochromatized Al Kα radiation (1486.6 eV). The X-ray spot size was 50 µm^2. Peaks were recorded with a constant pass energy of 23 eV. The binding energy scale was calibrated from the C 1s peak at 284.8 eV. The peaks are fitted with a Shirley background [27]. Parameters such as peak area ratio, the difference between the binding energy of the doublets, and the Full Width at Half Maximum (FWHM) were fixed for titanium contributions according to [28]. The peaks were analyzed and fitted using CasaXPS software [29]. A digital optical microscope (Keyence VHX - Z100R) was used to image the anodized surface at the same area as the EBSD measurements. Cross-sections at the boundary of areas with different colors were made with a FIB with a Dual Beam FEI Helios 600i microscope and observed with a STEM detector, part of the Dual Beam system (FEI STEM III detector). The electron beam acceleration voltage was 30 kV, in immersion mode. Energy-dispersive X-ray Spectroscopy (EDX) analyses were performed in a Zeiss Supra FEG SEM microscope, with an Oxford Instrument system, at an accelerating voltage of 30 kV. Transmission Kikuchi Diffraction (TKD) was used in the SEM mentioned above to analyze the crystallographic orientation of the grains on which the oxide layer has grown on the FIB lamellae.

2.4. Optical model for the simulation of the color

Optical simulations were carried out to compute the color, taking into account the internal morphology of the oxide layer revealed by FIB lamellae preparation and subsequent analysis. Color can be predicted from the reflectance spectrum [5]. To achieve this, reflectance spectra were first simulated using the Abeles matrix formalism [30], which is based on the transfer matrix method employed to analyze the propagation of electromagnetic waves through a layered medium. The medium is assumed to be composed of a homogeneous oxide layer and a semi-infinite Ti substrate located in air. The two interfaces are plane and parallel, which means that the surface is assumed to be smooth (no roughness) and the oxide thickness is assumed to be constant. The input parameters

are the refractive indexes of the oxide layer and substrate, the oxide thickness and the angle of incidence. The oxide thickness is selected based on STEM observations of the FIB lamellae. The incident light angle is fixed at 0° corresponding to the geometry of the optical microscope. In fact, certain colors, known as gonioapparent, can change depending on the angle of observation [31]. As the angle of incidence increases, the position of the extrema of the associated reflectance spectrum shifts towards shorter wavelengths, resulting in a perceived change in color. In the case of a heterogeneous oxide layer (for example, porosity or inclusions of a different oxide), a homogeneous effective refractive index n_{eff} is calculated through the Maxwell-Garnett approximation [32] from a material of refractive index n_m containing inclusions of refractive index n_i (Figure 2), where f is the filling factor:

$$n_{eff}^2 = n_m^2 \frac{1 + \frac{2}{3} f\gamma}{1 - \frac{1}{3} f\gamma} \tag{1}$$

$$\gamma = \frac{n_i^2 - n_m^2}{n_m^2 + \frac{1}{3}(n_i^2 - n_m^2)} \tag{2}$$

Figure 2: Schematic representation of a heterogeneous oxide layer modeling by computing a homogeneous effective refractive index through the Maxwell-Garnett approximation.

To compute the color, the simulated reflectance spectra were then converted into CIE 1931 XYZ chromaticity coordinates [33] assuming a D65 illuminant [34]. XYZ tristimulus values for colored stimuli are calculated with the following equations:

$$X = k \int_{380nm}^{780nm} \phi_\lambda(\lambda)\bar{x}(\lambda)\,\mathrm{d}\lambda, Y = k \int_{380nm}^{780nm} \phi_\lambda(\lambda)\bar{y}(\lambda)\,\mathrm{d}\lambda, Z = k \int_{380nm}^{780nm} \phi_\lambda(\lambda)\bar{z}(\lambda)\,\mathrm{d}\lambda \tag{3}$$

where $\phi_\lambda(\lambda)$ is the spectral distribution of the illuminant, $\bar{x}(\lambda)$, $\bar{y}(\lambda)$, and $\bar{z}(\lambda)$ are the color matching functions of the CIE 1931 standard observer [33], and k is a normalization constant.

Subsequently, XYZ values were converted into sRGB color coordinates [35] to display their colors digitally as described in [36]. The relationship between XYZ and sRGB D65 is the following:

$$\begin{bmatrix} R \\ G \\ B \end{bmatrix} = \begin{bmatrix} 3.2406 & -1.5372 & -0.4986 \\ -0.9689 & 1.8758 & 0.0415 \\ 0.0557 & -0.2040 & 1.0570 \end{bmatrix} \begin{bmatrix} X \\ Y \\ Z \end{bmatrix} \tag{4}$$

where the X and Z represent the color chromaticity and Y represents the color brightness.

3. Results

3.1. Substrates

EBSD analyses of the substrates, with and without HF/HNO_3 etching, reveal a two-phase, equiaxed microstructures (Figures 3a and 4a). The studied unetched substrate area is composed of 95% α phase and 3.3% β phase, with 1.7% not indexed, which is representative of an equiaxed Ti-6Al-4V alloy. The studied etched substrate area is composed of 84% α phase and 14.7% β phase, with 1.3% not indexed. The non-indexed areas probably still have residual stresses despite vibratory polishing. This same zone was also analyzed by EBSD before etching, and the distributions of the α and β phases before and after etching are compared in Figure 5. Before etching, the percentage of α/β phases for this area was 93/7%, and after etching, it was 84/14.7%. Hydrofluoric acid dissolves titanium dioxide by forming a titanium fluoride complex that is soluble in solution and nitric acid limits the dissolution reaction by a competing chemical oxidation reaction due to nitrate ions [37]. Fluoro-nitric etching of titanium is commonly used to remove the native oxide layer, known as α-case, and therefore by revealing the microstructure

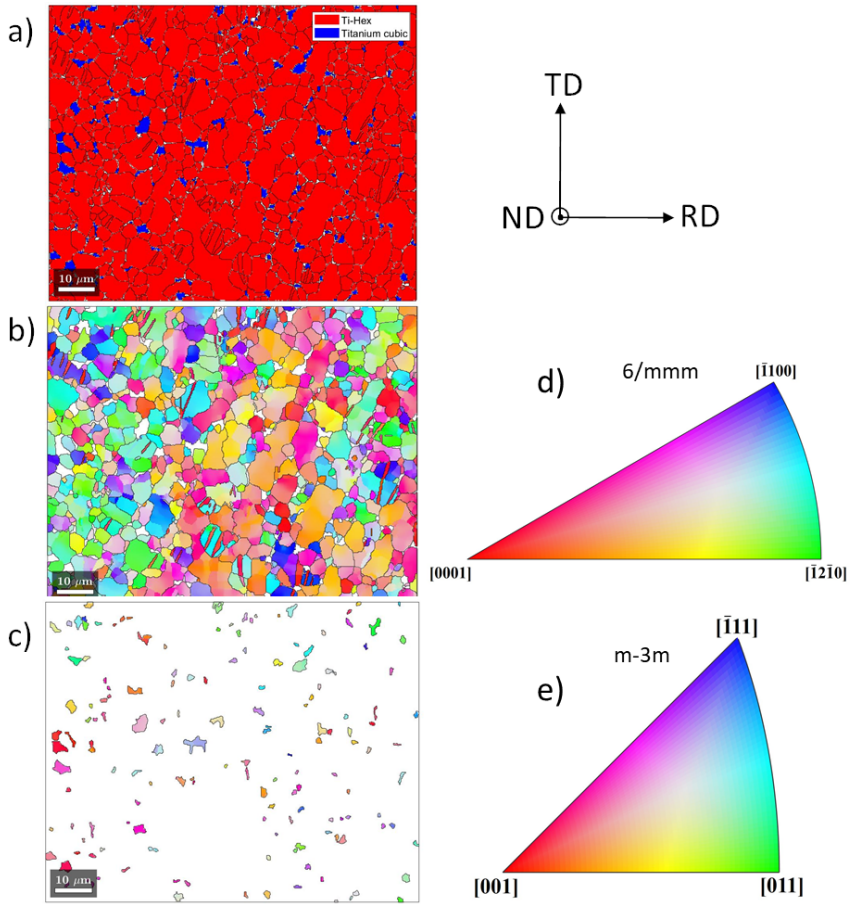

Figure 3: (a) α (red) and β (blue) phases indexing of the unetched Ti-6Al-4V substrate. Maps of the crystallographic planes normal vectors for (b) the α phase and (c) the β phase and (d,e) associated inverse pole figure color codes.

[38]. The STEM observations done on a FIB lamella (Figure 10) show that the prismatic plane $(01\bar{1}0)$ is more etched than the basal plane (0001). The HF/HNO_3 etching is thus non-uniform and this could explain the α/β phase repartition change after etching. The change of the α/β phase composition at the substrate surface could also be due to an inhomogeneous volume repartition of the two phases. Furthermore, Vermesse et al. [39] showed by X-ray diffraction (XRD) analysis that the internal stresses of a rolled Ti-6Al-4V substrate decrease after HF/HNO_3 etching. It would be pertinent to investigate the internal stresses associated with the α and β phases on the rolled Ti-6Al-4V substrate before and after HF/HNO_3 etching to determine the effect of internal stresses on chemical etching.

The EBSD results presented in Figures 3 and 4 are those obtained along the vector normal to the (RD,TD) plane, as this is the growth direction of the oxide layer. Maps of the crystallographic orientations of the α and β phases separately and the associated reverse pole color code are shown in Figure 3 for the unetched substrate and in Figure 4 for the etched substrate.

3.2. Oxide layers

3.2.1. Chemical composition

Anodic oxides on Ti-6Al-4V are often referred to as primarily consisting of titanium dioxide TiO_2 [4]. However, the chemical composition of the film can be affected by alloying elements, which are also oxidized during the electrochemical oxidation process. For instance, Zwilling et al. [40] demonstrated that the oxide layer on Ti-6Al-4V alloy is enriched in aluminum oxide Al_2O_3 with a Ti/Al atomic ratio similar to 5. Comparison with other studies is difficult due to the variety of experimental conditions, such as electrolyte, substrate, and anodization voltage. To

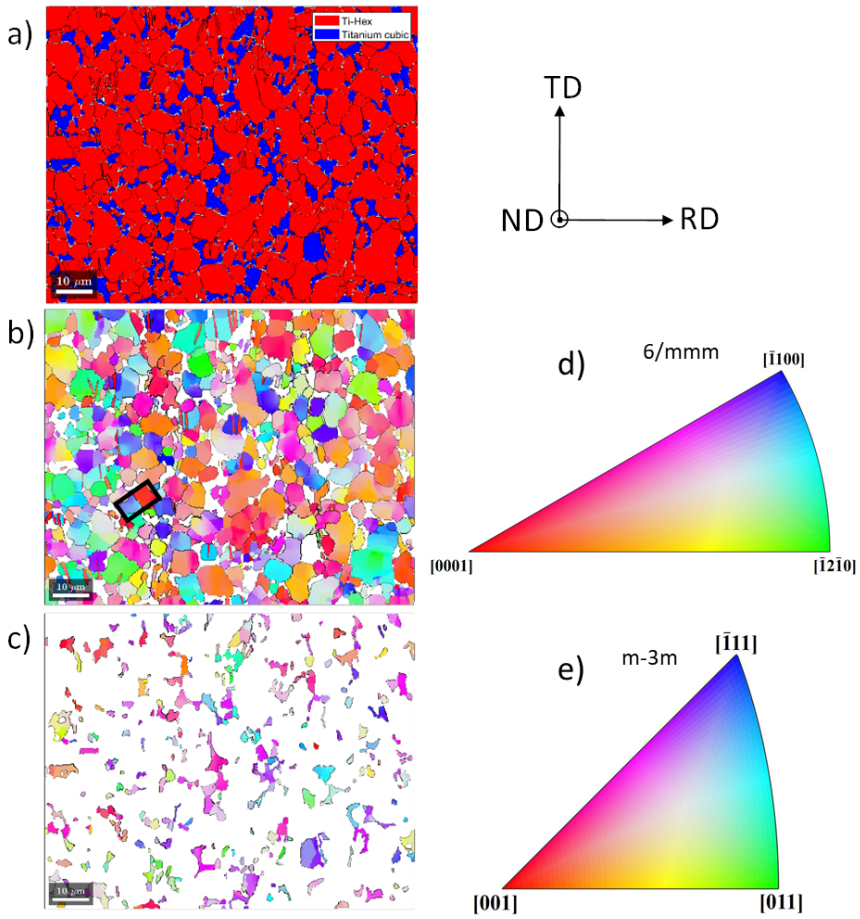

Figure 4: (a) α (red) and β (blue) phases indexing of the etched Ti-6Al-4V substrate. Maps of the crystallographic planes normal vectors for (b) the α phase and (c) the β phase and (d,e) associated inverse pole figure color codes. The black rectangle in subfigure (b) highlights two grains where the FIB lamella was realized.

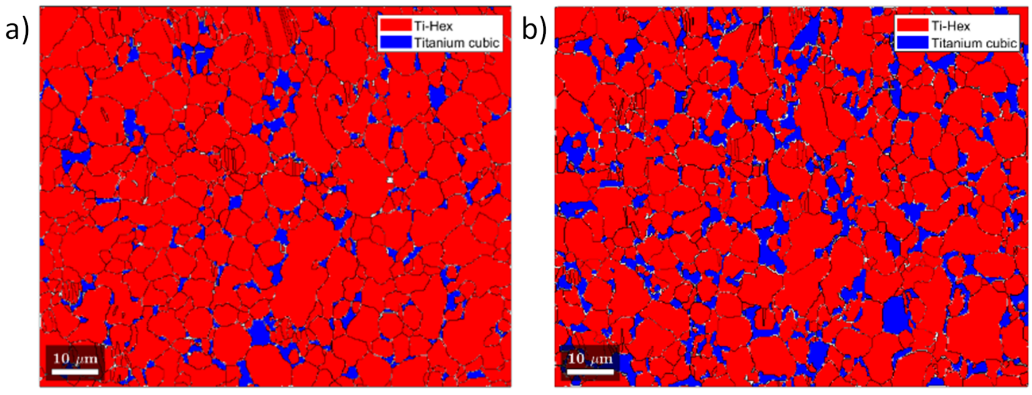

Figure 5: EBSD maps of the distribution of the α (red) and β (blue) phases over the same area (a) before and (b) after HF/HNO_3 chemical etching. The zone is the same as on Figure 3.

determine the chemical composition of the oxide layer formed under our conditions, an XPS analysis of the anodized Ti-6Al-4V was carried out. The high-resolution XPS spectra of Ti 2p, O 1s and Al 2p are shown in Figure 6. The binding energies of Ti $2p_{3/2}$ and Ti $2p_{1/2}$ are centered at 458.2 eV and 463.9 eV respectively (Figure 6a), showing that the oxide layer formed is indeed titanium oxide in the form of TiO_2, in agreement with the values for TiO_2 obtained in the literature [28]. The FWHMs are 2.17 and 1.27 for the Ti $2p_{3/2}$ and Ti $2p_{1/2}$ peaks respectively. The residual standard deviation is 1.3. The O 1s spectra were split into three peaks (Figure 6b): the dominant peak at 529.6 eV corresponds to the lattice O^{2-} in TiO_2, the peak at 531.6 eV was attributed to the lattice O^{2-} in Al_2O_3 and hydroxide bonding and the peak at 532.3 eV is attributed to organic oxygen species [28]. The peaks were fitted with a mixture of 70% Gaussian and 30% Lorentzian shapes. The FWHMs are 1.3 for the lattice oxide peak in TiO_2 and 1.5 for the other two peaks. The residual standard deviation is 1.3. The binding energy at 73.3 eV is attributed to the Al $2p_{3/2}$ corresponding to the presence of Al^{3+}. However, it should be noted that the presence of both titanium oxide and aluminum oxide shifts the binding energy of Ti^{4+} and Al^{3+} towards the lower side of the binding energy [41]. Vanadium was not detected. The quantification of the elements present in the layer, calculated from the area of the peaks weighted by the relative sensitivity factor, is presented in Table 2. The Ti/Al atomic ratio is similar to 6, close to that found by Zwilling et al. [40]. The oxide layer is therefore composed of 92 mol% TiO_2 and 8 mol% Al_2O_3. Although this analytical technique only probes the first few nanometres, it is assumed that the oxide layer consists of 92 mol% TiO_2 and 8 mol% Al_2O_3 throughout the thickness of the oxide layer.

Table 2: Atomic percentage of elements present on the surface of the anodized Ti-6Al-4V thin film measured by XPS analysis.

Elements	C	Ti	Al	$O^{(1)}$	$O^{(2)}$	$O^{(3)}$	impurities
Binding energy (eV)	284.8	458.2	73.3	529.6	531.6	532.3	—
Anodized Ti-6Al-4V	31 at%	12 at%	2 at%	35 at%	9 at%	5 at%	6 at%

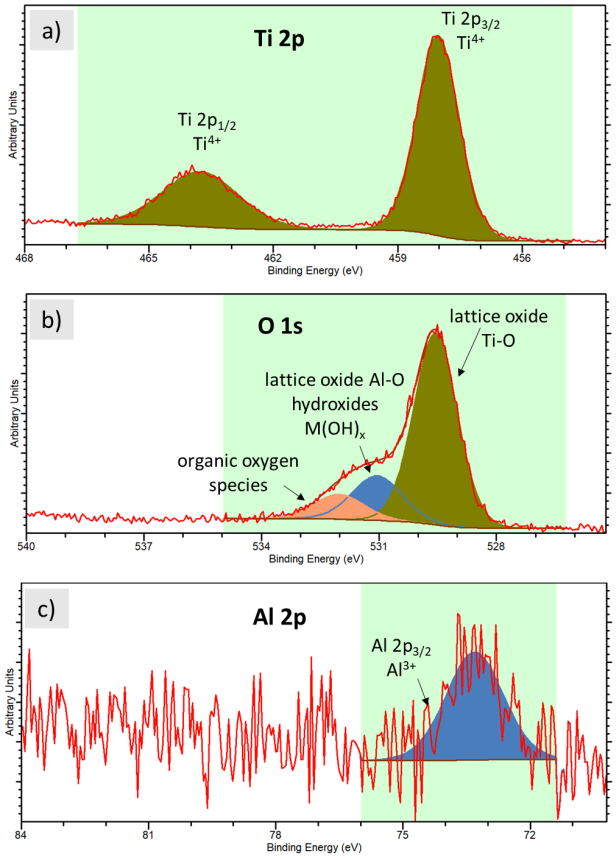

Figure 6: The high-resolution XPS spectra for (a) Ti 2p, (b) O 1s and (c) Al 2p.

3.2.2. Color

After anodizing, the samples exhibit a yellow color at the macroscopic scale. However, observation under an optical microscope reveals the presence of color inhomogeneities, as observed in other studies [4][21]. In our case, blue areas can be distinguished from the predominant yellow areas (Figure 7b for the ANOD-50V sample and Figure 8b for the ANOD-50V-HF sample). Note that the proportion of blue areas in the ANOD-50V-HF sample is lower than in the ANOD-50V sample. In addition, optical observation of the ANOD-50V-HF sample highlights the grain boundaries, certainly due to the higher surface roughness after anodizing caused by the chemical etching (S_a = 30 nm for ANOD-50V and S_a = 140 nm for ANOD-50V-HF).

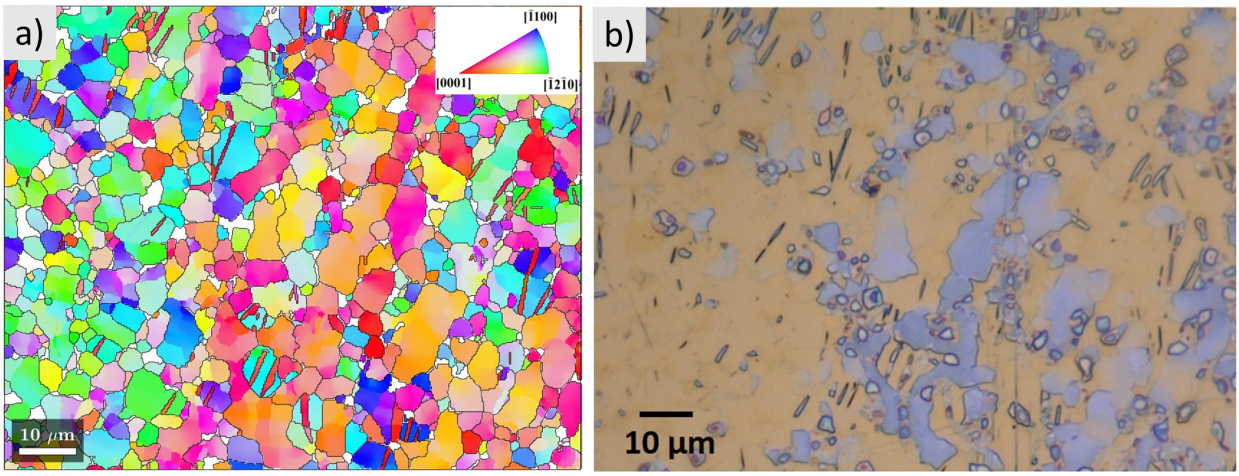

Figure 7: (a) Map of the crystallographic planes normal vector for the α phase with the associated inverse pole figure color code and (b) optical image of the ANOD-50V sample on the same area as (a) after anodizing.

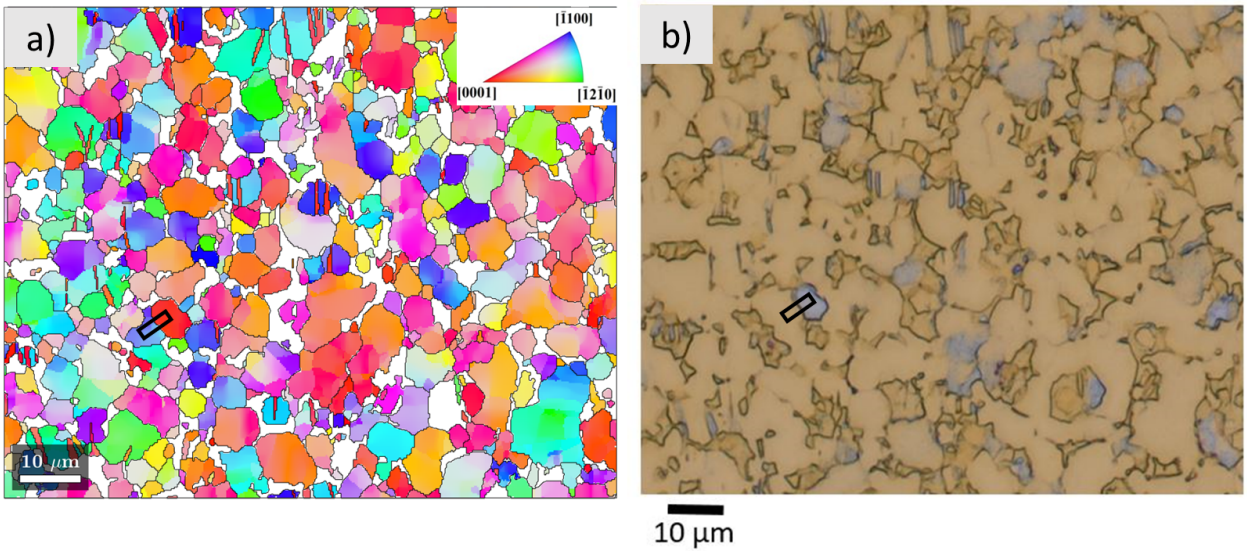

Figure 8: (a) Map of the crystallographic planes normal vector for the α phase with the associated inverse pole figure color code and (b) optical image of the ANOD-50V-HF sample on the same area as (a) after anodizing. The black rectangle corresponds to the area where the FIB lamella was done.

3.2.3. Morphology

Figure 9a shows the STEM observation of the FIB lamella of the oxide layer taken at the boundary of yellow and blue areas and the EDX analysis of the Ti, V and Al elements for the ANOD-50V sample (the position where the FIB lamella was made is not mentioned in Figures 3 and 7 because it was made in an area different from that

studied by EBSD for technical reasons). An inhomogeneous structure can be seen on the left side of the oxide layer, which appears blue, while the oxide layer is homogeneous on the right side, which appears yellow. It should also be noted that this change in morphology occurs close to a grain boundary in the substrate. EDX analysis of this area revealed the presence of an α grain on the left and a β grain on the right. Moreover, a TKD analysis of the FIB lamella identified the crystallographic orientation of the α grain under the oxide layer as (0001), while the β phase was not indexed (Figure 9b). In addition, EDX line scan analyses through the oxide layer were carried out on an inhomogeneous (blue arrow) and homogeneous (yellow arrow) zone. Figure 9c shows the evolution of oxygen through the oxide layer at both locations. For the inhomogeneous part, a drop in oxygen was highlighted in the black areas of the oxide layer in the STEM image, suggesting the presence of porosity. Oxygen is also present on the Ti-6Al-4V substrate because the latter is highly reactive with oxygen, so it naturally formed an oxide layer when it came into contact with air after the FIB lamella was made. Oxygen is less present on the C deposit because it is chemically inert.

A FIB lamella was also realized on the ANOD-50V-HF sample at the boundary of yellow and blue areas (the position of the FIB lamella is represented by the black rectangle in Figure 8). Again, a porous oxide layer is visible when the area is blue. In addition, a height difference of about 270 nm can be seen between the underlying grains of the blue and yellow areas (Figure 10), induced by chemical etching, which has dissolved certain phases preferentially to others, creating a higher surface roughness. The TKD analysis of the ANOD-50V-HF sample shows that here the areas of different colors have both grown on α phase grains but with different crystallographic orientations: the yellow area (homogeneous oxide layer) is above a grain with crystallographic orientation $(01\bar{1}0)$ and the blue area (inhomogeneous oxide layer) is above a grain with crystallographic orientation (0001). These results are in agreement with those obtained in the same area by EBSD before anodizing (Figure 4b, black rectangle).

The thickness of the oxide layer is visually estimated from the FIB lamella. For the ANOD-50V sample, the thickness of the oxide layer is 121 $\pm$ 3 nm and 118 $\pm$ 2 nm for the heterogeneous and the homogeneous oxide layers respectively. For the ANOD-50V-HF sample, the thickness of the oxide layer is 122 $\pm$ 2 nm and 123 $\pm$ 1 nm for the heterogeneous and the homogeneous oxide layers respectively. The percentage of porosity within the inhomogeneous layer is estimated by thresholding the oxide layer from the image of the FIB lamella using ImageJ software [42] (Figure 11) and corresponds to the ratio of the number of white pixels to the total number of pixels times one hundred. The percentage of porosity estimated from the FIB lamellae is 42% for the ANOD-50V sample and 51% for the ANOD-50V-HF sample.

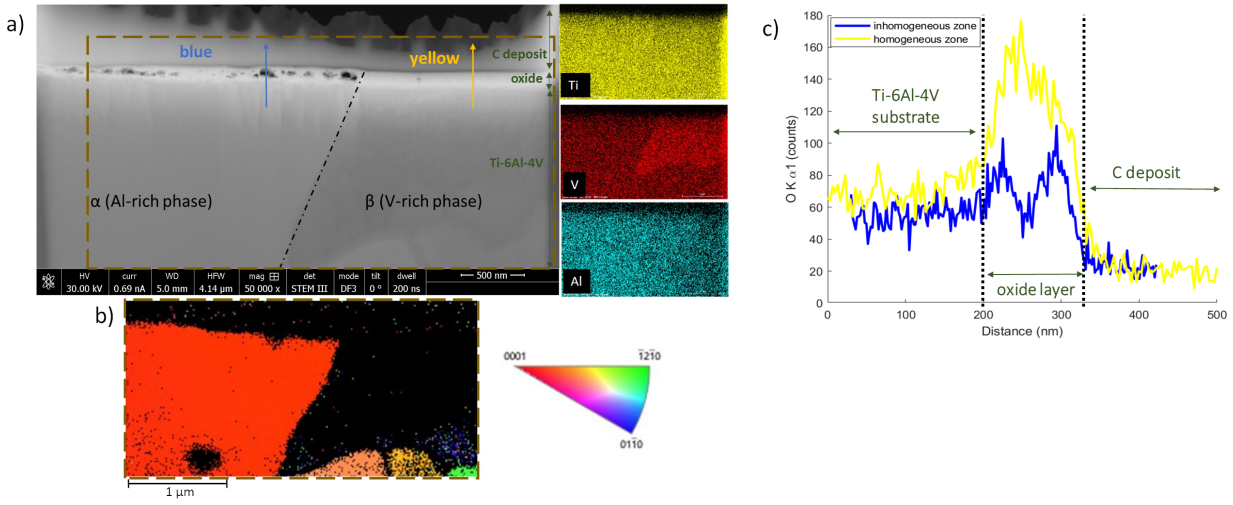

Figure 9: (a) STEM observation of the FIB lamella and associated EDX analyses of the Ti, V and Al elements for the ANOD-50V sample; the brown dotted lines identify the area studied by TKD (b) Map of the crystallographic planes normal vectors of the α phase of the FIB lamella obtained by TKD analysis and associated inverse pole figure color code; (c) EDX line scan of the Kα 1 line of oxygen within the oxide layer.

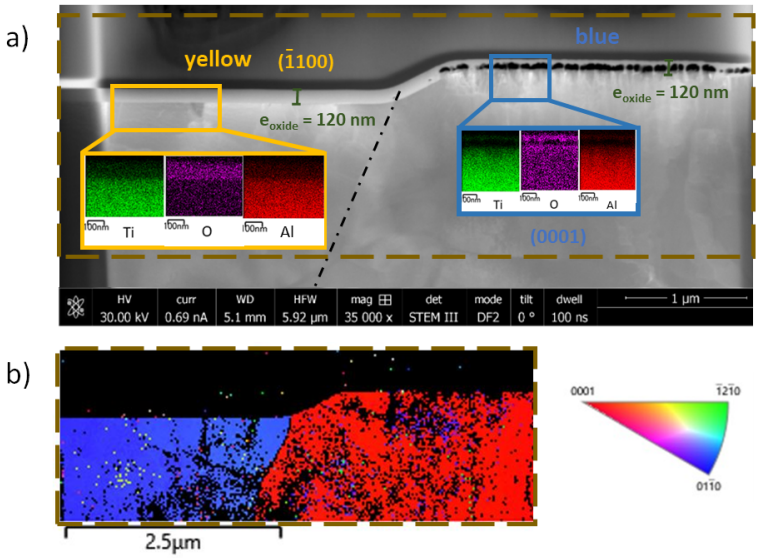

Figure 10: (a) STEM observation of the FIB lamella and associated EDX analyses of the Ti, O and Al elements for the ANOD-50V-HF sample; the brown dotted lines identify the area studied by TKD (b) Map of the crystallographic planes normal vectors of the α phase of the FIB lamella obtained by TKD analysis and associated inverse pole figure color code.

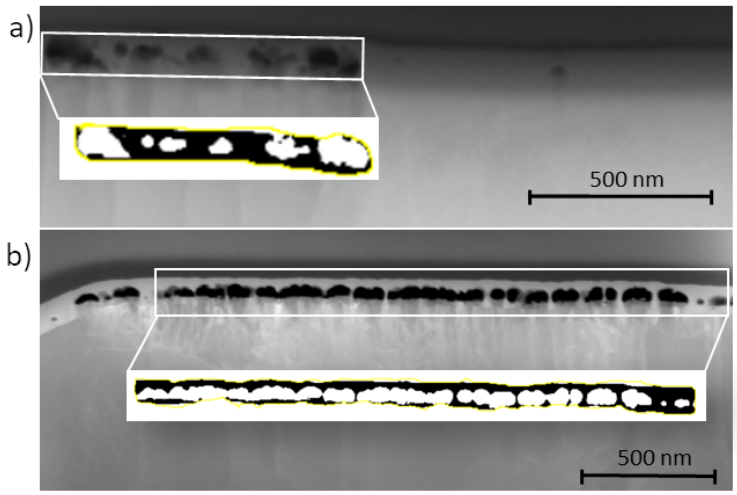

Figure 11: Threshold of the inhomogeneous part of the oxide layer of (a) the ANOD-50V sample and (b) the ANOD-50V-HF sample used to estimate the percentage of porosity using ImageJ software.

4. Discussion

4.1. Correlation between crystallographic orientation and color

By comparing the optical image of the anodized samples with the distribution of the α and β phases of the substrates (Figures 3a and 7b for the ANOD-50V sample and Figures 4a and 8b for the ANOD-50V-HF sample), it can be seen that the distribution of the yellow and blue zones does not correspond to the distribution of the α and β phases. Moreover, oxide layer on β grains always appears yellow. The blue zones are exclusively present on α grains. Then, by comparing the optical image of the anodized samples with the map of the crystallographic orientations of the α phase (Figure 7 for the ANOD-50V sample and Figure 8 for the ANOD-50V-HF sample), a trend emerges: grains perceived as blue are present on grains of crystallographic orientation (0001) or close to

it, while the remaining grains are yellow. These results are consistent with those reported by Vera et al. [4] and Diamanti et al. [21].

4.2. Origin of color variation

In the case of interference colors, the possible sources of color variability can be the thickness of the oxide layer and the structure of the oxide layer (chemical composition, crystallinity, and porosity).

Diamanti et al. [21] have determined the thickness of the oxide layer through reflectometry measurements on samples made at different anodizing voltages. They established a calibration between color and thickness, as the resolution of reflectometry measurements exceeded the size of individual grains. They have shown that the oxide layer formed on α-grains with crystallographic orientations close to (0001) is thinner compared to other crystallographic orientations. Their approach involved assuming a dense TiO_2 layer to obtain the thickness of the oxide layer from reflectometry measurements. However, the morphological insights provided by the FIB lamellae in the present paper (Figures 9 and 10) showed that the thickness of the oxide layer remains constant at about 120 nm for both yellow and blue oxide layers. Moreoever, the FIB lamellae revealed that the oxide layer exhibits porosity in the case of a (0001) crystallographic orientation of the α phase of the substrate.

The XPS analysis indicates that the oxide layer is a mixed oxide composed of 92 mol% TiO_2-8 mol% Al_2O_3. It should be noted that the XPS analysis covers a surface area of 50 μm^2, representing an average over both yellow and blue grains. The α and β grains have different chemical compositions [43] which might lead to oxide layers with locally varied chemical compositions. However, the observed color variation does not correspond with differences between α and β grains; instead, it correlates with specific crystallographic orientations of the α phase. So the color variation does not appear to be attributed to variations in the percentage of oxidized alloying elements.

The refractive index of the mixed oxide (92 mol% TiO_2-8 mol% Al_2O_3) was calculated using the Maxwell-Garnett approximation (Section 2.4) where n_m is the refractive index of TiO_2 from [24] and n_i is the refractive index of Al_2O_3 extracted from [44] with a filling factor of 0.08. Figure 12 shows the evolution of the refractive indexes of titanium, TiO_2 and Al_2O_3 used in the simulations of the reflectance spectra.

Following the observation of the heterogeneous internal morphology of the oxide layer on grains with a crystallographic orientation of (0001) (Figures 9a and 10a) and EDX analyses suggesting porosity due to the absence of chemical elements (Figures 9c and 10a), optical simulations of the color were carried out based on the model presented in Section 2.4, where in this case n_m is the refractive index of the 92 mol% TiO_2-8 mol% Al_2O_3 mixed oxide and n_i is the refractive index of air. The medium is assumed to be composed of a homogeneous porous mixed oxide layer, determined through the Maxwell-Garnett approximation and a semi-infinite Ti substrate located in air. The thickness of the oxide layer was set at 120 nm based on STEM observations of the FIB lamella.

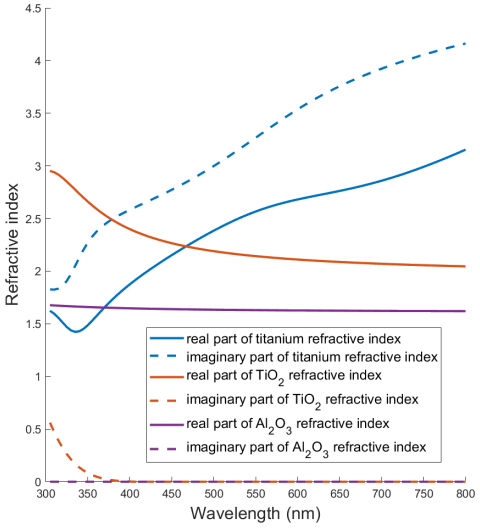

Figure 12: Refractive indexes of titanium, TiO_2 [24] and Al_2O_3 [44] used in the reflectance spectra simulations.

Figure 13 shows the simulated color evolution of a 120 nm thick oxide layer over a semi-infinite Ti substrate as a function of the oxide porosity, using the Maxwell-Garnett approximation. These simulations confirm a variation in

color as a function of porosity for a constant oxide thickness. This variation is attributed to the fact that porosity within the oxide layer reduces the effective refractive index. For instance, using the equations (1) and (2), for λ = 500 nm, n_m(92 mol% TiO_2-8 mol% Al_2O_3) = 2.14 and n_i = 1, so γ = -1.06. Therefore, regardless of the filling factor f, n_{eff} is necessarily lower than the refractive index n_m (for f=0.5, n_{eff}=1.59). Furthermore, these results are in agreement with the percentage of porosity estimated through image analysis of the porous zone from the FIB lamellae and the color perceived under the optical microscope.

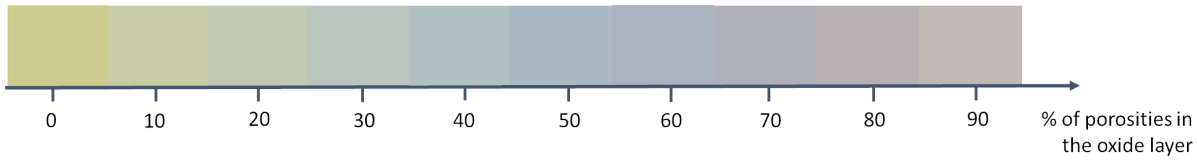

Figure 13: Simulations of the color of a 92 mol% TiO_2-8 mol% Al_2O_3 mixed oxide on Ti substrate as a function of the percentage of porosity for an oxide layer thickness of 120 nm.

In addition, the crystallinity of the oxide layer can change the refractive index. Figure A.1 shows the evolution of the refractive indexes of amorphous and anatase TiO_2 extracted from [6] and used in the simulations of reflectance spectra. Optical simulations were carried out to analyze the color of a 120 nm thin film of 100% amorphous TiO_2 (Figure A.2a) and a 120 nm thin film of 100% anatase TiO_2 (Figure A.2b). It can be seen that the variation in refractive indexes between amorphous and anatase TiO_2 is small and therefore the crystallinity has a negligible effect on the color.

4.3. Influence of grain orientation on porosity of the oxide layer

Observation of the morphology of the oxide layer on the FIB lamellae, coupled with the crystallographic orientation of the substrate on which the oxide layer was formed, has revealed a direct correlation between the presence of porosity and the crystallographic orientation (0001) of the α phase of the substrate. Kudelka et al. [45] have shown that the formation of the oxide layer on grains with a crystallographic orientation in the basal plane (0001) is slower than on grains in the transverse planes (hki0), in relation to the atomic density of the crystalline structure. The atomic density, defined as the ratio of the number of atoms in the periodic lattice of indexes hkl to the area of the periodic lattice of indexes hkl, is $\frac{2}{\sqrt{3}}\ \frac{1}{a^2} = \frac{1.154}{a^2}$ for the basal plane (0001) and $\frac{1}{ac} = \frac{0.63}{a^2}$ for the prismatic plane $(01\bar{1}0)$ (the lattice parameters of α Ti are a=0.2952 nm and c=0.4679 nm, with $\frac{c}{a} = \sqrt{\frac{8}{3}}$). Using cyclovoltammograms of oxide formation, Kudelka et al. [45] have also shown that during anodic oxidation of grains oriented in the transverse planes (hki0) the current density remains constant as the anodizing voltage is increased up to the desired voltage, in contrast to a non-constant current density which decreases for grains oriented in the basal plane (0001). The same observation was made by Crawford et al. [22] for the growth of TiO_2 nanotubes on a Ti substrate, which is delayed for grains with orientations close to (0001) compared to other orientations. They explained that this crystallographic orientation dependence is related to the atomic density of the different Ti planes, which influences the nature of the electron and ion exchange between the Ti surface and the electrolyte solution, thus controlling the growth rate of the oxide layer. The orientation planes (0001) have a higher atomic density and therefore a higher concentration of donors. It means that electron transfer reactions (oxygen generation) are favored over ion transfer reactions (layer growth). Matykina et al. [46] have also confirmed the preferential oxygen generation in the anodic layer on titanium grains which tend to have a basal-like orientation. Thus, the morphology of the oxide layer is influenced by the crystallographic orientations of the substrate during anodizing.

5. Conclusions

Characterizations of Ti-6Al-4V substrates (with or without HF/HNO_3 etching) and the corresponding anodized oxide thin films have revealed an indirect link between the crystallographic orientation of the substrate and the observed color variation of anodized Ti-6Al-4V at the microscopic scale. These color inhomogeneities can be explained by the crystallographic orientations within the α phase of the substrate, which influence the growth characteristics of the oxide layer. Specifically, the oxide layer is porous and appears blue when it has grown on a grain with crystallographic orientation (0001) of the α phase, whereas it is dense and appears yellow on other

orientations of the α phase and on all the grains of the β phase. This difference in morphology is the origin of the observed color variation, as demonstrated by the simulations of the color for the same oxide thickness but with different percentages of porosity. Optical simulations have also shown that the variation in the crystallinity of the oxide has a negligible effect compared to porosity on the color variation. These results highlight the significant impact of substrate crystallographic orientations on the morphology of the oxide layer produced by anodizing and, consequently, on the microscopic scale color variations in anodized Ti-6Al-4V.

Acknowledgements

This work was supported by the LABEX MANUTECH-SISE (ANR-10-LABX-0075) of Université de Lyon, within the Plan France 2030 operated by the French National Research Agency (ANR) and the realization of the FIB lamellae was made possible thanks to the contribution of MANUTECH-USD.

References

[1] M.V. Diamanti, B. Del Curto, and M.P. Pedeferri. Interference colors of thin oxide layers on titanium. *Color Research & Application*, 33:221–228, 2008.

[2] L. Bartlett. Variability in coloured titanium surfaces for jewellery. *PhD thesis, University of the Arts London*, 2009.

[3] S. Van Gils, P. Mast, E. Stijns, and H. Terryn. Colour properties of barrier anodic oxide films on aluminium and titanium studied with total reflectance and spectroscopic ellipsometry. *Surface and Coatings Technology*, 185(2-3):303–310, 2004.

[4] M.L. Vera, M.C. Avalos, M.R. Rosenberger, R.E. Bolmaro, C.E. Schvezov, and A.E. Ares. Evaluation of the influence of texture and microstructure of titanium substrates on TiO2 anodic coatings at 60 V. *Materials Characterization*, 131:348–358, 2017.

[5] M. Maillet, Q. Cridling, M. Lenci, M.P. Pedeferri, and R. Charrière. Multi-angle color prediction of glossy anodized titanium samples through the determination of the oxide layer structural parameters. *Journal of the Optical Society of America. A, Optics, image science, and vision*, 38:1065–1074, 2021.

[6] A. Jolivet, C. Labbé, C. Frilay, O. Debieu, P. Marie, B. Horcholle, F. Lemarié, X. Portier, C. Grygiel, S. Duprey, W. Jadwisienczak, D. Ingram, M. Upadhyay, A. David, A. Fouchet, U. Lüders, and J. Cardin. Structural, optical, and electrical properties of tio2 thin films deposited by ald: Impact of the substrate, the deposited thickness and the deposition temperature. *Applied Surface Science*, 608:155214, 2023.

[7] P. Chowdhury, Harish C. Barshilia, N. Selvakumar, B. Deepthi, K.S. Rajam, Ayan Roy Chaudhuri, and S.B. Krupanidhi. The structural and electrical properties of tio2 thin films prepared by thermal oxidation. *Physica B: Condensed Matter*, 403(19-20):3718–3723, 2008.

[8] B. Zhou, X. Jiang, R. Shen, and A.V. Rogachev. Preparation and characterization of tio2 thin film by thermal oxidation of sputtered ti film. *Materials Science in Semiconductor Processing*, 16(2):513–519, 2013.

[9] A. Pérez del Pino, J.M. Fernandez-Pradas, P. Serra, and J.L. Morenza. Coloring of titanium through laser oxidation: comparative study with anodizing. *Surface Coatings Technology*, 187:106–112, 2004.

[10] C.H. Heo, S-B. Lee, and J-H. Boo. Deposition of tio2 thin films using rf magnetron sputtering method and study of their surface characteristics. *Thin Solid Films*, 475(1-2):183–188, 2005.

[11] M.H. Suhail, G. Mohan Rao, and S. Mohan. dc reactive magnetron sputtering of titanium-structural and optical characterization of tio2 films. *Journal of Applied Physics*, 71(3):1421–1427, 1992.

[12] L. Miao, P. Jin, K. Kaneko, A. Terai, N. Nabatova-Gabain, and S. Tanemura. Preparation and characterization of polycrystalline anatase and rutile tio2 thin films by rf magnetron sputtering. *Applied Surface Science*, 212:255–263, 2003.

[13] M.V. Diamanti, B. Del Curto, and MP. Pedeferri. Anodic oxidation of titanium: From technical aspects to biomedical applications. *Journal of Applied Biomaterials and Biomechanics*, 9(1):55–69, 2011.

[14] M.V. Diamanti, B. Del Curto, V. Masconale, C. Passaro, and M.P. Pedeferri. Anodic Coloring of Titanium and Its Alloy for Jewels Production. *Color Research and Application*, 37:384–390, 2012.

[15] N.T. Sahrin, R. Nawaz, F.K. Chong, S.L. Lee, and M.D.H. Wirzal. Current perspectives of anodized tio2 nanotubes towards photodegradation of formaldehyde: A short review. *Environmental Technology Innovation*, 22:101418, 2021.

[16] K.W. Kang, S. Limandri, G. Castellano, S. Suarez, and J. Trincavelli. Thickness determination of anodic titanium oxide films by electron probe microanalysis. *Materials Characterization*, 130:50–55, 2017.

[17] M.V Diamanti, P. Pozzi, F. Randone, B. Del Curto, and M.P. Pedeferri. Robust anodic colouring of titanium: Effect of electrolyte and colour durability. *Materials and Design*, 90:1085–1091, 2016.

[18] T. Wang, L. Wang, Q. Lu, and Z. Fan. Changes in the esthetic, physical, and biological properties of a titanium alloy abutment treated by anodic oxidation. *The Journal of Prosthetic Dentistry*, 121(1):156–165, 2019.

[19] H. Hlinka, K. Dostalova, K. Cabanova, R. Madeja, K. Frydrysek, J. Koutecky, Z. Rybkova, K. Malachova, and O. Umezawa. Electrochemical, biological, and technological properties of anodized titanium for color coded implants. *Materials*, 16(2):632, 2023.

[20] E.M. Safwat, S.A. Abdel-Gawad, M.A. Shoeib, and S. El-Hadad. Electrochemical anodization of cast titanium alloys in oxalic acid for biomedical applications. *Frontiers of Chemical Science and Engineering*, 18(1):2, 2024.

[21] M.V. Diamanti, M.P. Pedeferri, and C.A. Schuh. Thickness of Anodic Titanium Oxides as a Function of Crystallographic Orientation of the Substrate. *Metallurgical and Materials Transactions A*, 39(9):2143–2147, 2008.

[22] G. A. Crawford and N. Chawla. Tailoring TiO2 nanotube growth during anodic oxidation by crystallographic orientation of Ti. *Scripta Materialia*, 60(10):874–877, 2009.

[23] S. Leonardi, V. Russo, A. Li Bassi, F. Di Fonzo, T.M. Murray, H. Efstathiadis, A. Agnoli, and J. Kunze-Liebhäuser. TiO2 Nanotubes: Interdependence of Substrate Grain Orientation and Growth Rate. *ACS Applied Materials & Interfaces*, 7(3):1662–1668, 2015.

[24] Q. Cridling, R. Charriere, D. Jamon, M. Lenci, M. Pedeferri, and D. Delafosse. Anodized titanium oxide thickness estimation with ellipsometry, reflectance spectra extrema positions and electronic imaging: importance of the interfaces electromagnetic phase-shift. *Thin Solid Films*, 709:138181, 2020.

[25] ACNIS Group. Ti-6al-4v – grade 5. `https://acnis-titanium.com/wp-content/uploads/2020/05/FR-TA6V-ELI_FT001.pdf`.

[26] F. Niessen, T. Nyyssönen, A.A. Gazder, and R. Hielscher. Parent grain reconstruction from partially or fully transformed microstructures in mtex. *J. Appl. Crystallogr.*, 55:180–194, 2022.

[27] S. Tougaard. Practical guide to the use of backgrounds in quantitative xps. *Journal of Vacuum Science Technology A*, 39:011201, 2021.

[28] M.C. Biesinger, L.W.M. Lau, A. Gerson, and R.St.C. Smart. Resolving surface chemical states in xps analysis of first row transition metals, oxides and hydroxides: Sc, ti, v, cu and zn. *Applied Surface Science*, 257:887–898, 2010.

[29] N. Fairley, V. Fernandez, M. Richard-Plouet, C. Guillot-Deudon, J. Walton, E. Smith, D. Flahaut, M. Greiner, M. Biesinger, S. Tougaard, D. Morgan, and J. Baltrusaitis. Systematic and collaborative approach to problem solving using x-ray photoelectron spectroscopy. *Applied Surface Science Advances*, 5:100112, 2021.

[30] F. Abeles. The generalized theory of thin films. *J. Phys. Radium*, 11:307–309, 1950.

[31] Q. Cridling. Influence of the substrate surface preparation on optical properties and color of anodized titanium. *PhD thesis, University of Lyon*, 2018.

[32] J.C. Maxwell Garnett. Colours in Metal Glasses, in Metallic Films, and in Metallic Solutions. II. *Philosophical Transactions of the Royal Society of London Series A*, 205:237–288, 1906.

[33] J. Schanda. *Colorimetry: Understanding the CIE System*. Wiley, 2007.

[34] CIE 2022, CIE standard illuminant D65, International Commission on Illumination (CIE), Vienna, Austria, DOI: 10.25039/CIE.DS.hjfjmt59.

[35] G. Sharma. *Digital Color Imaging Handbook*. CRC Press, 2002.

[36] N.P. Kirillova and T.M. Sileva. Colorimetric analysis of soils using digital cameras. *Genesis and Geography of soils*, 72:13–20, 2017.

[37] E.M.M. Suter and G.J. Goetz-Grandmont. The behaviour of titaniul in nitric-hydrofluoric acid solutions. *Corrosion Science*, 30:461–476, 1990.

[38] L.M. Gammon, R.D. Briggs, J.M. Packard, K.W. Batson, R Boyer, and C.W. Domby. Metallography and microstructures of titanium and its alloys. *ASM Handbook: Mettallography and Microstructures*, 9:899–917, 2004.

[39] E. Vermesse, C. Mabru, and L. Arurault. Surface integrity after pickling and anodization of ti-6al-4v titanium alloy. *Applied Surface Science*, 285:629–637, 2013.

[40] V. Zwilling, E. Darque-Ceretti, A. Boutry-Forveille, D. David, M. Y. Perrin, and M. Aucouturier. Structure and physicochemistry of anodic oxide films on titanium and ta6v alloy. *Surface and Interface Analysis*, 27:629–637, 1999.

[41] R. Tomaszek, L. Pawlowski, J. Zdanowski, J. Grimblot, and J. Laureyns. Microstructural transformations of tio2, al2o3+13tio2 and al2o3+40tio2 at plasma spraying and laser engraving. *Surface Coatings Technology*, 185:137–149, 2004.

[42] J. Schindelin, I. Arganda-Carreras, E. Frise, V. Kaynig, M. Longair, T. Pietzsch, S. Preibisch, C. Rueden, S. Saalfeld, B. Schmid, J-Y. Tinevez, D.J. White, V. Hartenstein, K. Eliceiri, P. Tomancak, and A. Cardona. Fiji: an open-source platform for biological-image analysis. *Nature Methods*, 9:676–682, 2012.

[43] Y. Qiao, D. Xu, S. Wang, Y. Ma, J. Chen, Y. Wang, and H. Zhou. Corrosion and tensile behaviors of ti-4al-2v-1mo-1fe and ti-6al-4v titanium alloys. *Metals*, 9(11):1213, 2019.

[44] S. Zhukovsky, A. Andryieuski, O. Takayama, E. Shkondin, R. Malureanu, F. Jensen, and A. Lavrinenko. Experimental demonstration of effective medium approximation breakdown in deeply subwavelength all-dielectric multilayers. *Physical Review Letters*, 115:177402, 2015.

[45] S. Kudelka, A. Michaelis, and J.W. Schultze. Effect of texture and formation rate on ionic and electronic properties of passive layers on Ti single crystals. *Electrochimica Acta*, 41:863–870, 1996.

[46] E. Matykina, R. Arrabal, P. Skeldon, G.E. Thompson, and H. Habazaki. Influence of grain orientation on oxygen generation in anodic titania. *Thin Solid Films*, 516:2296–2305, 2008.

Appendix A. Influence of crystallinity on color

Optical simulations were carried out for a 120 nm 100% amorphous TiO_2 layer (Figure A.2a) and a 120 nm 100% anatase TiO_2 layer (Figure A.2b). The refractive indexes used were taken from [6] for TiO_2 produced by ALD. The color variation induced by the difference in the crystallinity of the oxide layer is negligible compared to porosity. In fact, the refractive indexes between amorphous and anatase TiO_2 are close (Figure A.1).

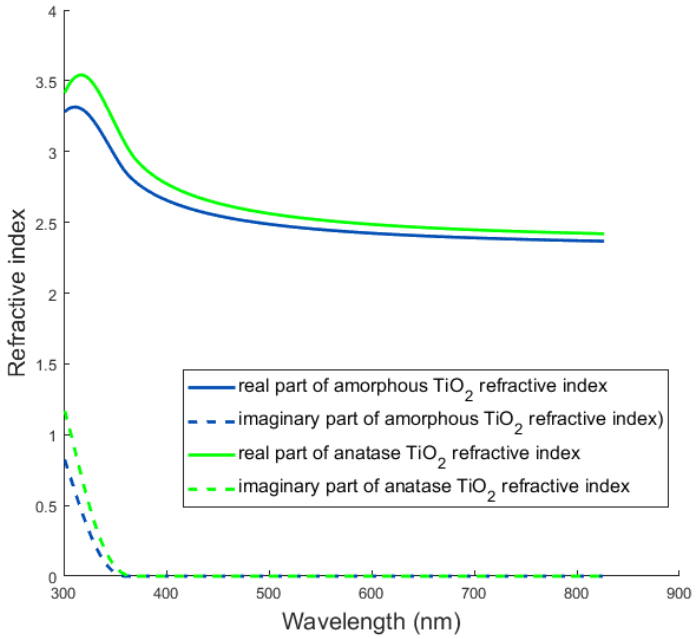

Figure A.1: Amorphous TiO_2 and anatase TiO_2 refractive indexes from [6] used in the reflectance spectra simulations.

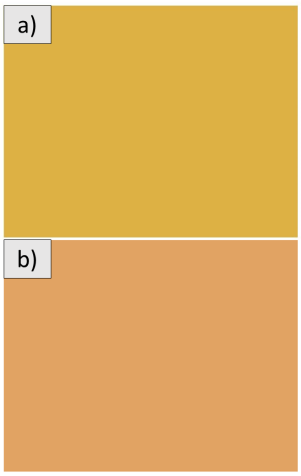

Figure A.2: (a) Simulations of the color of 120 nm of (a) 100% amorphous titanium oxide layer and (b) 100% anatase titanium oxide layer on Ti substrate.